Impact of Sn doping on the hydrogen detection characteristics of ZnO thin films: Insights from experimental and DFT combination

Zahira El Khalidi, Ayoub Daouli, Hicham Jabraoui, Bouchaib Hartiti, Amal Bouich, Bernabé Marí Soucase, Elisabetta Comini, Hashitha M.M. Munasinghe Arachchige, Salah Fadili, Philippe Thevenin, et al.

Impact of Sn doping on the hydrogen detection characteristics of ZnO thin films: Insights from experimental and DFT combination

Zahira El khalidi[1,2*], Ayoub Daouli[3,4], Hicham Jabraoui[5*], Bouchaib Hartiti[1], Amal Bouich[6], Bernabé Marí Soucase[6], Elisabetta Comini[7], Hashitha M. M. Munasinghe Arachchige[7], Salah Fadili[1], Philippe Thevenin[8], Abderrafi Kamal [9], Abdellatif Hasnaoui[4], Michael Badawi[3*]

[1] *MAC & PM Laboratory, FST Mohammedia, Hassan II Casablanca University Casablanca, Morocco*

[2] *University of Illinois at Chicago, Microphysics Laboratory, Chicago, IL 60607, USA*

[3] *Université de Lorraine, CNRS, Laboratoire de Physique et Chimie Théoriques, 54500 Nancy, France*

[4] *Université Sultan Moulay Slimane, LS3M, Faculté Polydisciplinaire de Khouribga, Khouribga, Morocco*

[5] *Université Paris-Saclay, CEA, CNRS, NIMBE, 91191 Gif-sur-Yvette, France*

[6] *School of Design Engineering, Universitat Politécnica de Valencia, Camí de Vera 46022, Spain*

[7] *Sensor Laboratory, University of Brescia, Valotti 7, 25123, Brescia, Italy*

[8] *Université de Lorraine, LMOPS, F-57500 Metz, France*

[9] Laboratoire de Physique de la Matière Condensée (LPMC), Faculté des Sciences Ben M'sik, Université Hassan II de Casablanca, Casablanca, Morocco

Corresponding authors:

E-mail addresses: zahira@uic.edu; hicham.jabraoui@cea.fr ; michael.badawi@univ-lorraine.fr

ABSTRACT

The development of efficient chemical sensors based on semiconductor oxides is a major challenge. Low-cost equipment fabrication with a high sensor response towards H_2 was the aim of our work. Chemical sensors were elaborated using zinc oxide, aluminum- and tin-doped zinc oxide. The samples were synthesized with a cost-effective chemical spray pyrolysis technique. Sn-doped ZnO response to hydrogen gas is the highest followed by ZnO and Al-doped ZnO, with a high sensitivity reaching 200 at 500 ppm, for 400°C. DFT calculations revealed that O_2 is strongly adsorbed on the ZnO-Al surface, resulting in the cancellation of the electrical conductance. Consequently, the approaching H_2 gas will not possess sufficient energy to extract the strongly adsorbed oxygen from the surface, and no trapped electrons can be released back to the surface. In contrast, DFT calculations highlighted the potential of ZnO and Sn-doped ZnO to be used as hydrogen gas sensors. Charge transfer analysis revealed that only a small release of the trapped electrons occurs on the pure ZnO surface (0.14|e|), compared to Sn doped ZnO, in which a full release of free electrons was observed, resulting in a more favorable response to H_2 and confirming the experimental results.

Keywords: Sn-doped ZnO, ZnO thin films, Synthesis, Characterization, TEM, XPS, DFT calculations

1. Introduction

Because of its advantages such as combustion efficiency and low density, hydrogen (H_2) could be classified as a source of clean and sustainable energy[1]. However, the storage and transportation of H_2 raised significant concerns, especially its leakage from pipelines [2]. The large explosive concentration range of dihydrogen[3]and the difficulty of its detection by human sensory organs[4] make it a threat for environmental safety. Therefore, an evaluation of H_2 concentration in the air, with a suitable gas sensor is required. Previous studies were conducted

to evaluate the efficiency of H_2 sensors [5,6]. However, a sensor that detects H_2 with a minimum detection/recovery time, high selectivity, and sensitivity is still needed. To ensure high sensor performance factors, semiconductor materials were suggested as the best alternatives in gas sensors technology [7]. Many semiconductor oxides like SnO_2 [8], TiO_2 [9], and NiO [10] have been studied, besides ZnO with its promising properties desired in many fields like photovoltaic energy [11], Bio-imaging or LEDs[12], and the detection of liquid or gaseous species [12,13].

ZnO can be synthesized using physical and chemical processes. In the physical deposition with the steam phase, the material's deposition is the result of condensation on a substrate by the jets of neutral or ionized molecules and atoms. Among the main physical processes used to develop thin layers, we cite: Sputtering [14], Pulser-laser Deposition [15], and other techniques that present a distinct advantage providing a high composition control, film thickness, and sharp transition. Despite all previous qualities, and in addition to the high operating system cost required by this process, other drawbacks remain, such as the need of the cooling system and skilled control of vacuum and temperature. For this purpose, researchers were attracted by chemical methods for their simplicity and low cost, besides the good adhesion of the layers and the porosity of the treated surfaces which is the basic quality needed for a better gas detection. In this category we cite: Sol-Gel [16] and Spray Pyrolysis [17].

In a recent research works, Kumar et al. [18] detected H_2 gas with a high percentage at 1000 ppm of the gas concentration, using ZnO thin films decorated by Au nanoparticles. Another work reported by Gaspera et al. [19] stated that the nanostructured ZnO doped thin films showed a higher response compared to intrinsic zinc oxide. Generally, doping exhibits a significant influence on the optoelectronic properties of materials [20]. In particular, and based on previous reports, the addition of Sn dopant increases the electrical conductivity of the host ZnO material. Free electrons are released without creating a huge lattice distortion during the substitution of Zn by Sn. Al dopant exhibited a similar influence on ZnO thin films and improved the sensing properties of the gas sensor by improving its response and reducing its response/recovery time as reported by Yoo et al. [21].

Our work aims to improve ZnO sensors using a straightforward experimental process. The basic outcome is to assess and improve hydrogen detection through the addition of Sn and Al. The experimental gas testing of Sn-doped ZnO exhibited high sensing performance compared to Al-

doped ZnO. Along with the experimental efforts, we performed density functional theory (DFT) calculations to understand, at the atomic scale, experimental results such as the poor response of Al-doped ZnO and the mechanism of H_2 gas detection by ZnO and explain how the Sn and Al affect the sensitivity of ZnO to reducing gas. The accuracy of DFT is sufficient to predict and understand interactions between organic molecules and solids in general ZnO-based gas detection mechanisms in particular [22–26]. The outcome and the novelty of our work is to assess and improve the hydrogen detection through the addition of Sn and Al to ZnO thin films. Our goal is to reach a high sensor response and interpret theoretically the low response observed for Al doped ZnO. Herein, the experimental gas testing of Sn-doped ZnO exhibited high sensing performance reaching 200 at 500 ppm, for 400°C compared to Al-doped ZnO, ZnO, and other previous works from literature. The low Al doped ZnO response was evaluated by the density functional theory (DFT) calculations and provided an atomic understanding of H_2 gas trapping by ZnO and explained how the Sn and Al affect the sensitivity of ZnO to reducing gas. The response we reached in our work, was higher at low gas target concentration, compared to some reports from literature such as Drmosh *et al* [54], who reached a response between 80-95, at the operating temperature of 300˚C, under a high gas concentration of about 1200 ppm. The other research work [55], that was recently published, the authors claimed that the gas response was around 13, with lower operating temperature 250˚C, but the gas concentration was above 1500 ppm.

The paper is organized as follows: first, we detail our experimental and computational procedures, then, the obtained results with both experimental and DFT tools are presented and discussed focusing on the explanation of the high and low sensitivity of Sn and Al-doped ZnO, respectively. Finally, we outline the main conclusions of our study.

2. **Materials and methods**

2.1 Experimental section

The chemical reagents used in the experiments are zinc chloride (Cl_2Zn, 98%), aluminum nitrate extra pure Al $(NO_3)_3.9H_2O$ and tin (II) chloride dehydrate, extra pure Ph Eur, DAB ($SnCl_2.2H_2O$) brought from SIGMA-ALDRICH. The deposition of thin films was performed

using a cost-effective chemical spray pyrolysis method. The substrate preparation and the deposition process were similar to our previous work[23]. Three aqueous solutions were prepared, containing distilled water and 0.05 M of zinc oxide powder. The first solution contains pure zinc oxide, the second and the third solutions containing respectively, zinc oxide with the ratios $[Sn^{4+}]/ [Zn^{2+}]$ = 4% and $[Al^{3+}]/ [Zn^{2+}]$ = 4% as precursors. Each solution was agitated for 30 min at 60°C.

2.2 Characterization of the elaborated thin films

The structural characterization of the samples was established with a monochromator X-Ray Diffraction (Diffractometer system = XPERT-PRO) using Cu-Kα radiation and a wavelength of 0.15406 nm. The voltage was maintained at 20 kV, the measurements were obtained according to Bragg's law, and the detector used was point on arm. The surface morphology of the thin films was identified using scanning electron microscopy (FEI Quanta 650 FEG Environmental). Scanning Electron Microscopy (SEM) system was set at an acceleration voltage of 25 kV. We used a HORIBA monochromator iHR320 to measure the Raman spectra. The system was configured at room temperature using a grating of 1800 gmm^{-1}, connected to a Peltier-cooled Synapse CCD. The He-Cd laser (442 nm) was targeting the sample by a fiber coupled optical microscope at 100× magnification. We selected the wavelength of 200–800 cm^{-1} range. A detailed description of the equipment are described concisely in our previous work [23]. We used High Resolution Transmission Electron Microscope 100 kV (TEM 100) to perform additional structural analysis. TEM (JEO-JEM-1010) measurement conditions were 2.5 kV at various magnifications. The X-ray photoelectron spectroscopy is (XPS, SPECS GmbH) type, using $Al_{K\alpha}$ X-rays with the same XRD wavelength.

2.3 Computational methodology

The detection performance of pure ZnO and Al/Sn doped ZnO surfaces to H_2 gas was investigated through the periodic density functional theory (DFT)[27,28]. Vienna Ab initio Simulation Package (VASP) is used to run our DFT calculations[29,30] , with a plane-wave basis set and projector augmented wave (PAW) [31,32] pseudopotential. The functional of Perdew, Burk, and Ernzerhof (GGA-PBE)[33] was combined with the Tkatchenko-Scheffler scheme with iterative Hirshfeld partitioning (TS/HI) [24,34] correction to account for dispersion

forces. The total energy convergence for the self-consistent [35] iterations was set to 10^{-6} eV. Gaussian smearing with a smearing width of 0.05 eV was considered for Brillouin-zone integrations on a 2×2×1 k-mesh. The geometry optimization was performed until the forces were smaller than 0.02 eV/Å per atom[29]. The adsorption energies of gaseous molecules on the ZnO surface have been calculated at 0 K according to the following equation, the same trend has been used in many works [24,35–38]:

$$\Delta E_{ads} = E_{(ZnO-gas)} - (E_{ZnO} + E_{gas}) \quad (1)$$

where $E_{(ZnO\text{-}gas)}$ is the energy of the ZnO (0002) surface with the adsorbate, E_{ZnO} and E_{gas} are the energies of the ZnO surface and the isolated molecule in the gaseous phase, respectively. The charge density difference (Δρ) and Bader charge[39–41] difference (ΔQ) have been determined to further improve our understanding of the interaction of molecules with pure and Al- or Sn-doped ZnO. To visualize the charge density difference (Δρ) (using VESTA[42]) introduced by the adsorption of H_2 and O_2 onto ZnO surfaces, we combine the three charge densities namely the density of the complex $\rho_{ZnO\text{-}gas}$, the density of the clean ZnO surface $\rho_{ZnO,}$ and the density of the isolated molecule in the gaseous phase ρ_{gas}, as shown in the equation below[43]:

$$\Delta\rho = \rho_{ZnO-gas} - \rho_{ZnO} - \rho_{gas} \quad (2)$$

To get the difference in Bader charge ΔQ, the following equation was used:

$$\Delta Q = Q_{ZnO-gas} - Q_{ZnO\&gas} \quad (3)$$

where $Q_{ZnO\text{-}gas}$ is the Bader charge of all atoms upon adsorption and $Q_{ZnO\&gas}$ is the Bader charge of the separated clean ZnO surface and the separated isolated molecule in the gaseous phase.

3. **Results and discussions**

The structural characterization of the samples is described in the XRD patterns (Figure.1). We observe multiple peaks corresponding to the wurtzite structure as indicated in (JCPDS card 36-1451)[44]. The highest electrons density is translated by the highest intensity along (002) direction, which is the preferred orientation of the polycrystalline ZnO. Other peaks

related to ZnO such as (220) and (222) appeared within the patterns, the other peaks proving the addition of Sn and Al are (511) and Sn (112) respectively.

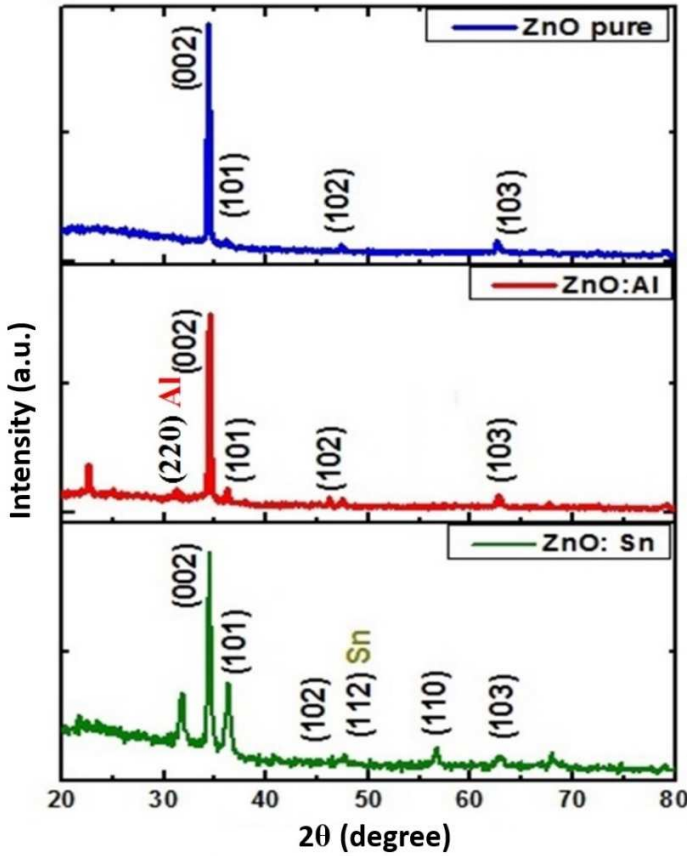

Figure 1. *X-Ray Diffraction patterns of ZnO, Al-doped ZnO, and Sn-doped ZnO thin films.*

The structural identifications of the samples can be determined by calculating the lattice constants a and c [45] (Eq. 4), the crystallite size D_{hkl} [46] (Eq. 5), and the dislocation density δ [47] (Eq. 6):

$$\frac{1}{d^2} = 4/3 \left(\frac{h^2+hk+k^2}{a^2}\right) + \frac{l^2}{c^2} \quad (4)$$

$$D = 0.9 \frac{\lambda}{\beta \cos\theta} \quad (5)$$

$$\delta = \frac{1}{D^2} \quad (6)$$

where (λ = 1.54 Å) is the incident radiation wavelength, θ represents the Bragg angle and β is the full width at half maximum (FWHM).

The results of the structural analysis are given in (Table 1) from which we observe that the dislocation is increasing while the crystallite size and lattice constants values are decreasing upon doping. This could be explained by the variation in the structure after the doping process, which leads to altering the film's crystallinity and the creation of mechanical stress caused by the substitution of Zn^{2+} with lower size Al^{3+} and Sn^{4+} ions [48].

Table 1: *Structural parameters of ZnO, Al, and Sn doped ZnO. JPCDS card N°: 36-1451 (a = 3.250 Å and c = 5.207Å).*

Sample	**d_{hkl} (002)**	**D(nm)**	**$\delta*10^5$ $(nm)^{-2}$**	**Lattice constants**		
				a(Å)	**c(Å)**	**c/a**
ZnO	2.6031	22.19	203.08	3.245	5.210	1.6055
ZnO:Al	2.6035	12.49	641.02	3.006	4.964	1.651
ZnO:Sn	2.6025	8.98	1240	3.001	4.942	1.646

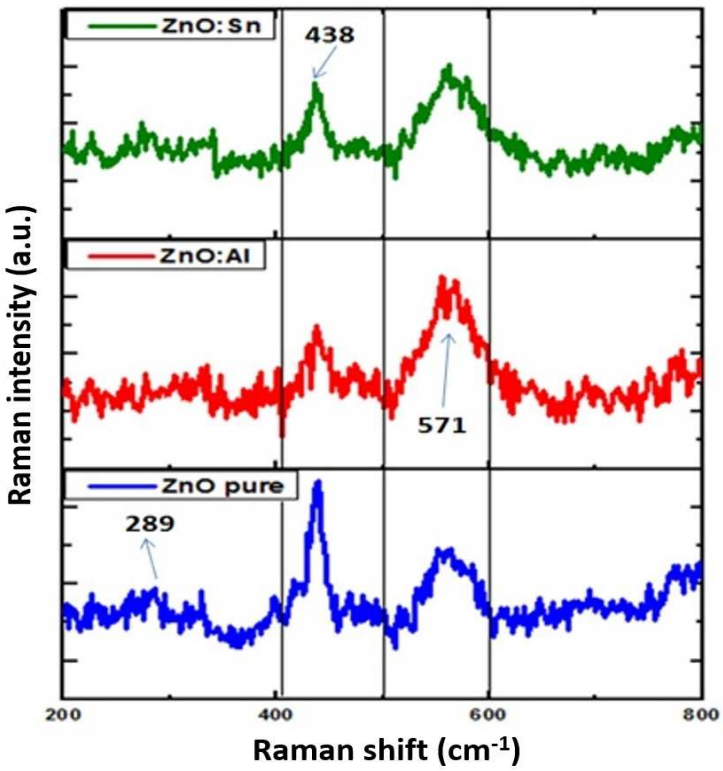

Figure 2. *Raman patterns of ZnO, Al-doped ZnO, and Sn-doped ZnO thin films.*

To confirm the XRD data, Raman spectroscopy characterization was performed to identify the vibrational modes in our samples. From (Figure 2), we can observe the existence of the conventional modes related to ZnO nanoparticles, precisely at 233, 289, and 338 cm^{-1} in the range from 200 to 400 cm^{-1}. The ZnO wurtzite mode is observed at 437 and 456 cm^{-1} according to the E_2 polar mode [49]. The Optical Longitudinal (OL) E_1 observed at 550 and 556 cm^{-1}, is attributed to the oxygen deficiency, where the multiphoton processes and resonance lead to well-resolved Raman peaks [50].

The variation of intensities and the translation in E_1 and E_2 modes from pure to doped ZnO can be explained by the increase in Al and Sn concentrations, with their ions occupy and substitute those of zinc in the lattice. This mechanism can be ascribed to the active and inactive Raman phonons regarding the lattice caused by Raman shift disorder.

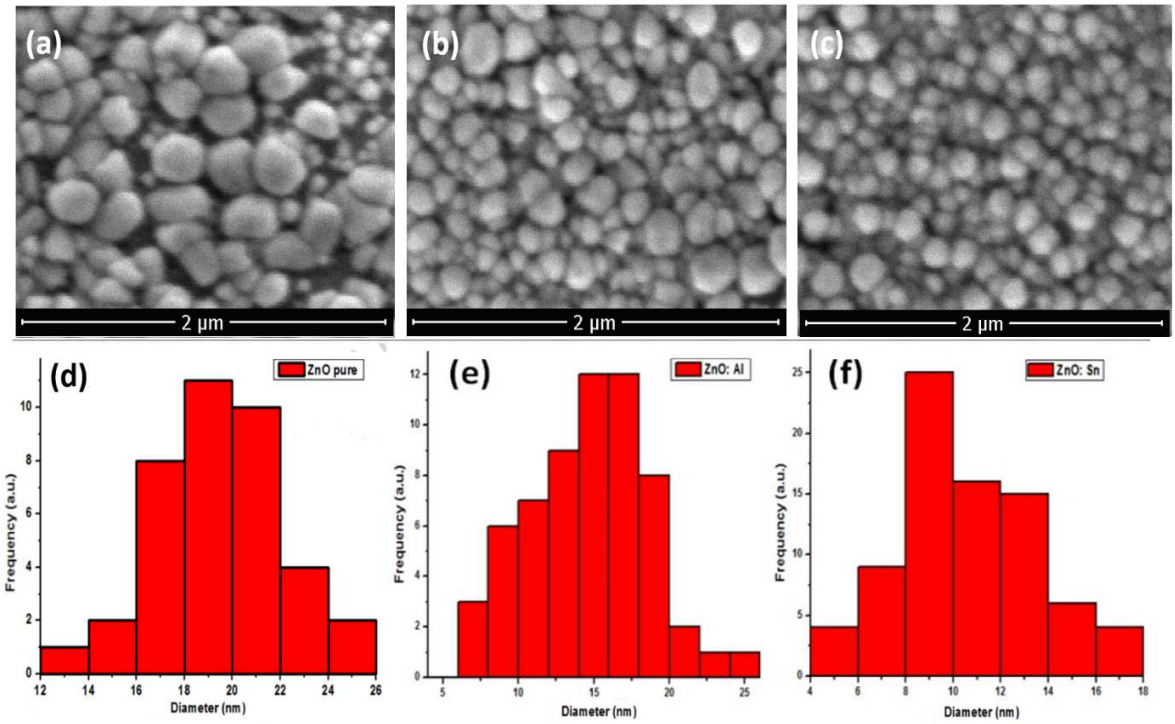

Figure 3. *SEM illustrations of a) ZnO, b) Al-doped ZnO, and c) Sn-doped ZnO thin films, and the corresponding grains diameter distribution (d, e, f).*

Scanning Electron Microscopy (SEM) micrographs (Figure 3) show the grains size distributions of pure and doped ZnO. Intrinsic zinc oxide exhibited the hexagonal structure shape at 2 µm, Sn and Al-doped ZnO showed porous morphology with smaller grain diameter lower than 18 nm. This surface is a good environment for the adsorption phenomenon.

High resolution transmission electron microscope (HRTEM) was also provided to characterize the microstructure of our films. The TEM mapping (Figure. 4, a, b, e, f, g) demonstrates the existence of Zn, O, Sn element in ZnO and Sn doped ZnO, and no results were reported for Al doped ZnO.

From the selected area electron diffraction (SAED) patterns presented in (Figure. 4, m), we observed that Sn doped ZnO exhibits good-crystalline structure without the appearance of stacking faults. In the same (Figure. 4, d, n, and O), HRTEM described the ordered lattice fringes

of both ZnO and Sn doped ZnO. From HRTEM image at a higher magnification, Sn doped Zn surface showed some disorder, and this might be due to oxygen vacancies. X-ray photospectroscopy (XPS) was performed to investigate the chemical state of the surface elements. From (Figure. 4, P), the intense peak located at 530.0 ± 0.1 eV is assigned to lattice oxygen bonded as O^{2-} ions in the ZnO matrix in our samples [51]. This means that the peak around 530 eV in O1s core level spectra corresponds to oxygen vacancies and the area under this peak gives feedback on vacancies. In this regard, Sn doped ZnO is found to have the largest surface area which means higher oxygen vacancies followed by ZnO and ZnO doped Al.

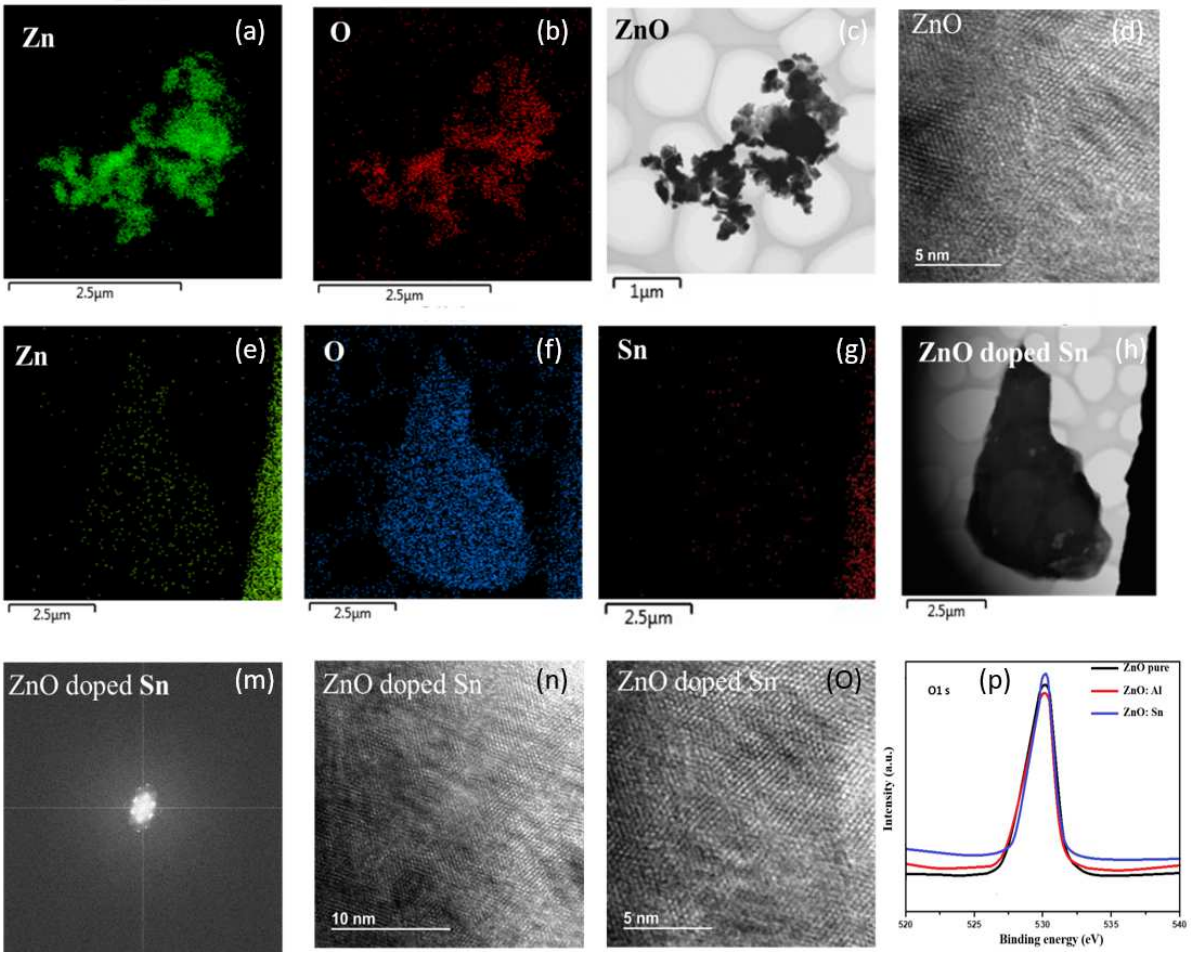

Figure 4. *EDS mapping of ZnO (a,b), and ZnO:Sn (e, f, g). HRTEM images of ZnO at 5nm (d). TEM images of ZnO (c), ZnO:Sn (h). SAED patterns of ZnO:Sn (m). ZnO:Sn at 10nm (n), 5nm (O). XPS O1s spectrum for all films (p).*

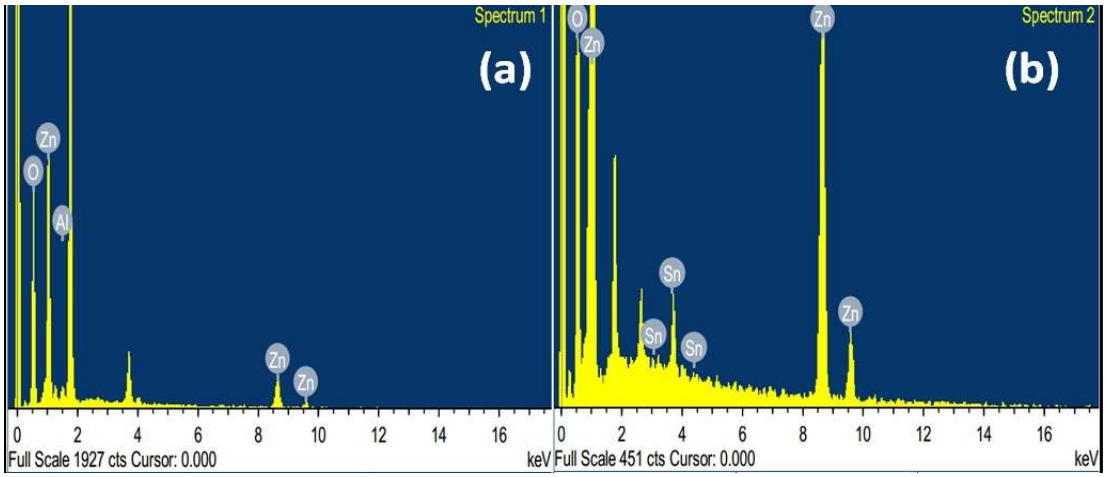

Figure 5. *EDS spectrums of a) ZnO: Al and b) ZnO: Sn.*

The energy-dispersive X-ray spectroscopy (EDS) was carried out to evaluate the atomic weight and the percentage of each element in ZnO, Al, and Sn-doped ZnO, respectively. Zn, O, Al and Sn are present in the samples, with the atomic weights: 59% (O), 37.9% (Zn), 3.1% (Sn), and 3.8 (Al). The high oxygen concentration could be explained by the addition of Al and Sn elements. These spectrums confirmed the existence of Sn and Al in the ZnO network.

The electrical measurements were also carried out using 4-point probe technique. We passed a current through two outer probes and reported the voltage through the inner probes. The electrical conductivity, resistivity, and conductance were calculated and presented in Table 2. The electrical resistivity was calculated using the following equation:

$$\rho = Bt\,V/I \quad (7)$$

where B = π / ln2, V is the voltage across inner probes, I is the current in outer probes, and t is the thickness of the thin films.

Table 2: *Resistivity and conductivity of ZnO and Sn doped ZnO thin films.*

Samples	Resistivity (Ω.cm)	Conductivity $(\Omega.cm)^{-1}$
ZnO	$63.01x10^{-4}$	158.7
ZnO:Sn	$62.39x10^{-4}$	160.28

From the table we can observe the decrease in the resistivity after doping with Sn. This decrease in resistivity is probably due to the number of free electrons from the Sn donor ions incorporated in the substitutional or interstitial locations of the Zn cations. Small amounts of the dopant (Sn) introduce into the ZnO network a large number of free carriers and in this case decrease the resistivity.

3.1 Application of gas sensors

3.1.1 Device fabrication

The thin films were deposited on alumina substrates to form the sensor device. Interdigitated contacts and the heaters were deposited to measure the resistance and conductance of the oxide materials. The adhesion layer was deposited by magnetron sputtering (70W argon plasma, 7 SCCM argon flow, 5.5 10^3 mbar at room temperature). The platinum contacts were placed using the same conditions to deposit the adhesion layer, and the device test was maintained in the temperature range (200˚C – 500˚C).

3.1.2 Sensor measurements

The response of the gas sensor was performed in an isolated chamber, the humidity was set at 50% with a gas flow reaching 200 sccm at 20˚C. The temperature of each sample was controlled, each target gas was added to a synthetic air (SIAD, Italy) to fix the target concentration. The voltage between (1V-10V) was applied to measure the conductance of the devices. The sensors were heated during 10 hours before introducing the gas, then, we expose them to the desired gas and concentration.

To measure the resistance of the sensor under the analyte gas, we deposit two or more electrodes on metal oxide materials. According to the type of the adsorbed gas and the charge carrier, the resistance may increase of decrease. For our n-type devices, a high amount of oxygen

is adsorbed on the sample surface and accept electrons from the material, decreasing its electron density and increasing its resistance.

The determination of the conductance variation is determined by the following expression:

$$S_i = \frac{\Delta R}{\Delta [B]_i} \quad (8)$$

S_i is the sensitivity of the gas, R the response of the sensor (the output of the sensor, resistance, or conductance, ...), $[B]_i$ is the concentration of the gas i.

The functional ZnO sensor device is presented in Figure 6.

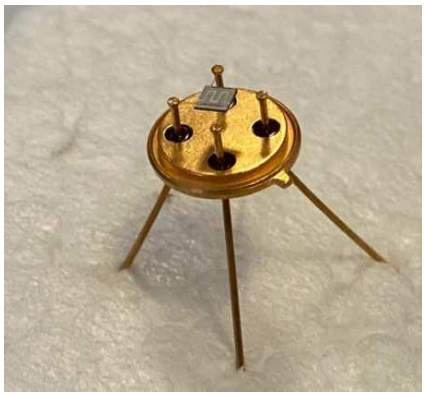

Figure 6. *The functional chemical sensor device of ZnO film.*

The films were exposed to H_2 flux, the conductance of the films increases due to the increase of the gas concentration. The sensor's response (Figure 7) is considered high under H_2 target gas, Sn doped ZnO shows a high response compared to pure ZnO for both low and high temperatures (Figure 8), followed by Al-doped ZnO that exhibited a very low response.

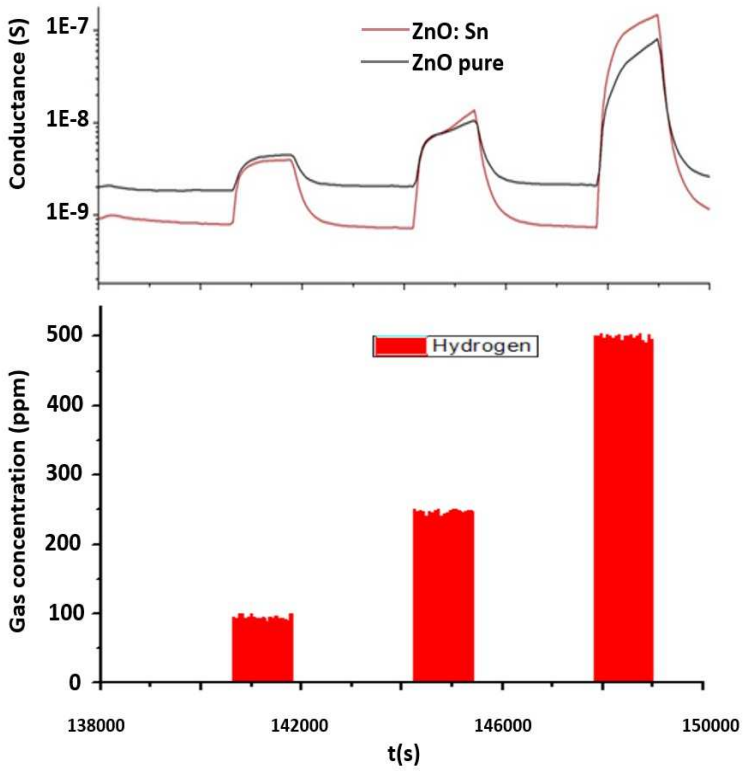

Figure 7. *Responses of Sn-doped ZnO and ZnO sensors under H_2 (100-250-500 ppm) at 400°C with corresponding humidity of 40% at 20°C.*

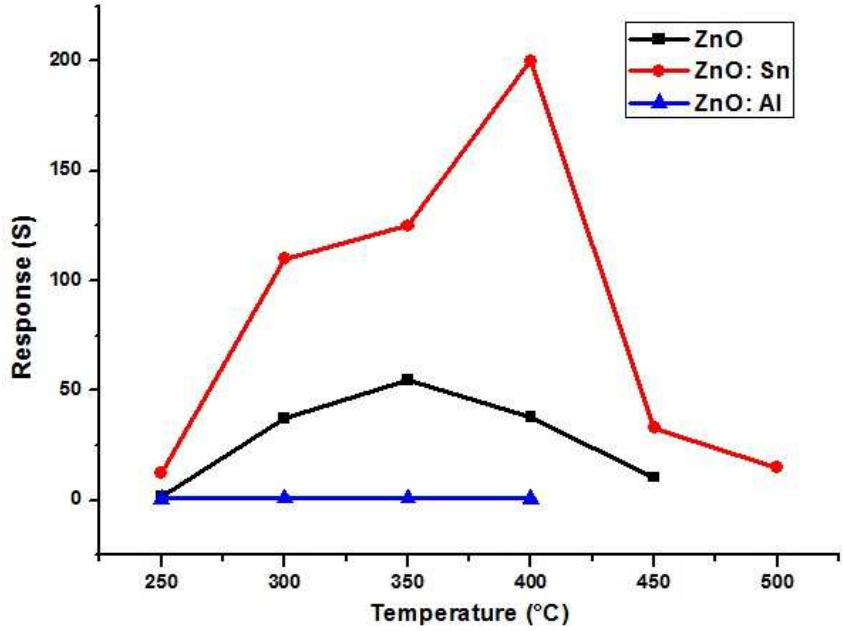

Figure 8. *Variation of response with the temperature of ZnO, ZnO: Sn, and ZnO: Al towards hydrogen (500 ppm) with corresponding humidity of 40% at 20°C.*

The optimal working temperature under 500 ppm of H_2 gas is 350°C for ZnO and 400°C for Sn-doped ZnO.

The variation of response/recovery time was calculated and presented in Table 3. Sn-doped ZnO showed lower values compared to literature [48], where the authors observed response/recovery times fluctuating between 312 s and 349 s using other dopants such as Pd and In_2O_3 [49].

Table 3: *Response and recovery times of the sensors ZnO, Al-doped ZnO and Sn-doped ZnO.*

Sample	Response time	Recovery time
ZnO	81	99
Sn-doped ZnO	50	80
Al-doped ZnO	79	101

The addition of 4 wt.% of Sn altered the sensing characteristics of the gas sensor, but the addition of Al decreased the response of the sensor. To explain this, we refer to the interpretation of the results detailed in the theoretical part.

3.2 DFT calculations

In this work, DFT calculations are employed to explain how the Sn and Al doping affect the sensitivity of ZnO (0002) towards H_2. The Zn-terminated polar ZnO (0002) surface was modeled by repeated slabs containing six ZnO double layers separated by a 20 Å vacuum slab along the (0002) direction (Figure 9). To avoid any artificial charge transfer between the bottom

oxygen layer and the top zinc layer (i.e., metallization effect), Hydrogen atoms with a nuclear charge of Z= 0.5|e| and an electron charge of 0.5 e were introduced to saturate the broken surface bonds on the bottom of the oxygen layer. The same procedure has been used by Kress [52]in his study of novel stabilization mechanisms on the ZnO (0001)-Zn polar surface.

The top three ZnO layers including the adsorbates have been relaxed, while the bottom four ZnO layers are kept fixed at their initial optimized bulk positions, with the equilibrium lattice constants of a = 3.281 Å and c = 5.306 Å (c/a=1.617; *ideal hexagonal structure shows c/a =1.633).* This is in good agreement with the experimental lattice parameters a=3.245 and c=5.210 (Table 1), and with values found by S. J. Pearton a= 3.249 Å and c = 5.206 Å [53].

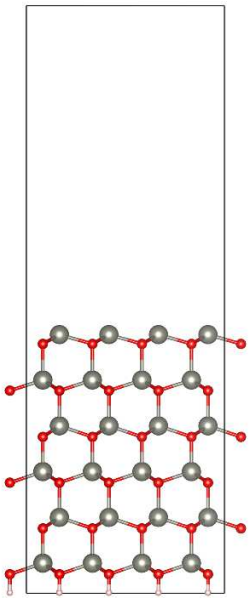

Figure 9. *Illustrations of the supercells of ZnO (0002)-Zn*

Color code: Zn is gray, and Oxygen is red.

3.2.1 Pure ZnO (0002) surface

The operating mechanism of gas sensors is mainly based on the change in electrical conductivity of the sensor caused by the transferred charge between the sensing materials and the gas molecules. The flow of electricity inside the sensing material is determined by the number of free electrons. It has been shown experimentally that when the sensing material is in clean air, the oxygen molecule (O_2) is adsorbed on the sensor surface, and the free electrons are extracted

from the conduction band. This results in the creation of O anion species, causing a change in the electrical conductance of the sensor. This means that the resistance of the sensor will increase, resulting in a decrease in the flow of electrons within the sensing material. Therefore, in the presence of reducing gases such as H_2, when it reacts with oxygen, the electrons generated upon adsorption of oxygen are released back into the sensing material. As a result, sensing resistance decreases, allowing more current.

The process involved in detecting H_2 gas at the ZnO (0002) surface can be described by the following reactions:

$$O_2 \text{ (air)} \rightarrow O_2 \text{ (adsorbed)} \quad (9)$$

$$O_2 \text{ (adsorbed)} + 2e \text{ (ZnO free electron)} \rightarrow 2\ O^- \quad (10)$$

$$2H_2 \text{ (reducing gases)} + 2O^- \rightarrow 2H_2O + 2e \text{ (ZnO free electron)} \quad (11)$$

We first investigated the interaction of O_2 and H_2 with the surface of ZnO (0002). The DFT calculations revealed that the H_2 molecule is mainly adsorbed by dispersion forces with a 54% dispersion contribution in total interaction energy of -19 kJ/mol, it was observed that the H_2 molecule interacts with the surface at 2.86 Å, leading to a charge transfer of only 0.08 |e| between the molecule (H_2) and the surface (Zn). However, when the O_2 molecule is adsorbed on the ZnO surface, a complex is created involving three Zn atoms from the surface, resulting in total interaction energy of -32.6 kJ/mol. We found that the interaction between O and Zn atoms presents a significant electron transfer of 0.58 |e| and an average interaction distance of 1.98 Å (Figure 10). This demonstrates that an oxygen anion layer is formed on the ZnO (0002) surface and therefore the formation of H_2O molecule is occurring (Eq.9). Due to this, a small release of trapped electrons to the surfaces of ZnO (0002) of 0.14 |e| is observed, which proves the potential of this material as a gas sensor. However, the responses are expected to be low, which implies a modification of the ZnO material.

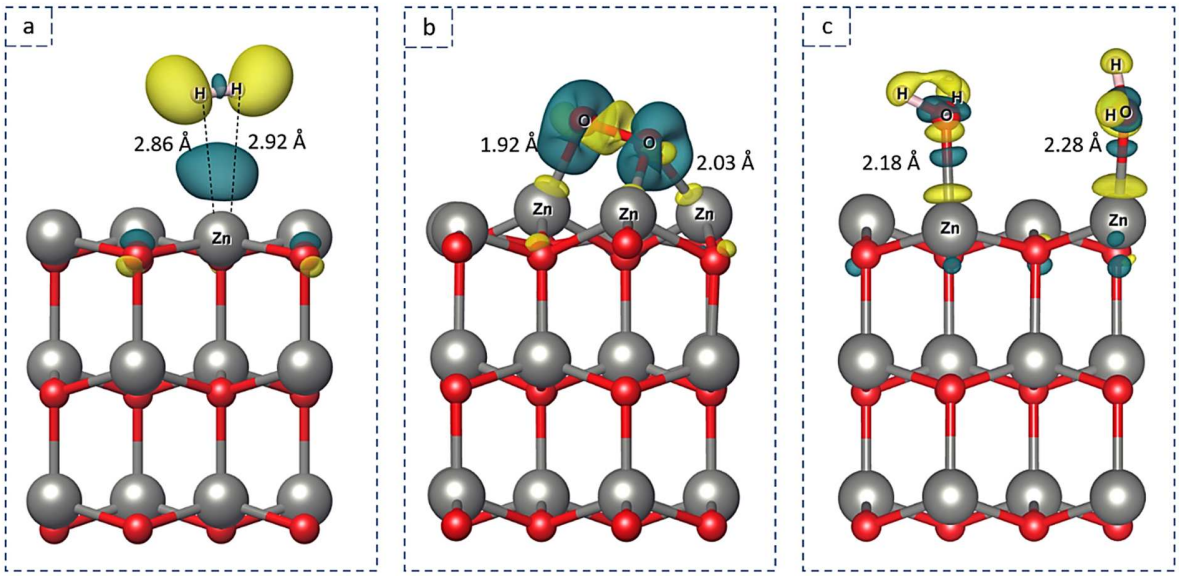

Figure 10. *Difference in electronic density (Δρ) induced by the adsorption of a) H_2 b) O_2 on pure ZnO (0002) surface, c) the attack of H_2 on the adsorbed O_2. The blue (yellow) zones correspond to the increase (decrease) in density.*

3.2.2 Al and Sn-doped ZnO

To account for direct contact between the dopants and the molecules, we have substituted a Zn atom of the upper layer by either Al or Sn atoms. After the relaxation of these two structures, we found that aluminum and tin are bound to oxygen atoms with an average distance of 1.81 Å (See Figure 11), 2.15 Å (See Figure 12) respectively, compared to that of Zn-O (1.92 Å).

3.2.3 Al-doped ZnO

Concerning the adsorption of H_2 molecule, the total interaction energy is (-121 kJ/mol), this high energy is caused by the dissociative adsorption of the molecule. The difference in charge density revealed that no interaction persists between the two H_2 atoms upon adsorption (Figure 10). This means that even in the absence of O_2 in the air, the H_2 molecule can extract

electrons from the conduction band of the Al-doped ZnO, resulting in the cancellation of the electrical conductance.

In the presence of oxygen molecules, we found that the aluminum atom of the surface strongly interacts with the O_2, leading to its dissociation into two oxygen ions. The electron density ($\Delta\rho$) and Bader charge (ΔQ) differences revealed that this dissociation presents a significant electron transfer of 1.31 |e| between the O and Al atoms. Therefore, the approaching H_2 gases cannot extract the strongly adsorbed oxygen, and only 0.08 |e| is released back to the surface. Hence, no H_2O formation will occur.

This weakens the H_2 detection signal and explains the extremely low response of ZnO-Al to hydrogen (Figures 8).

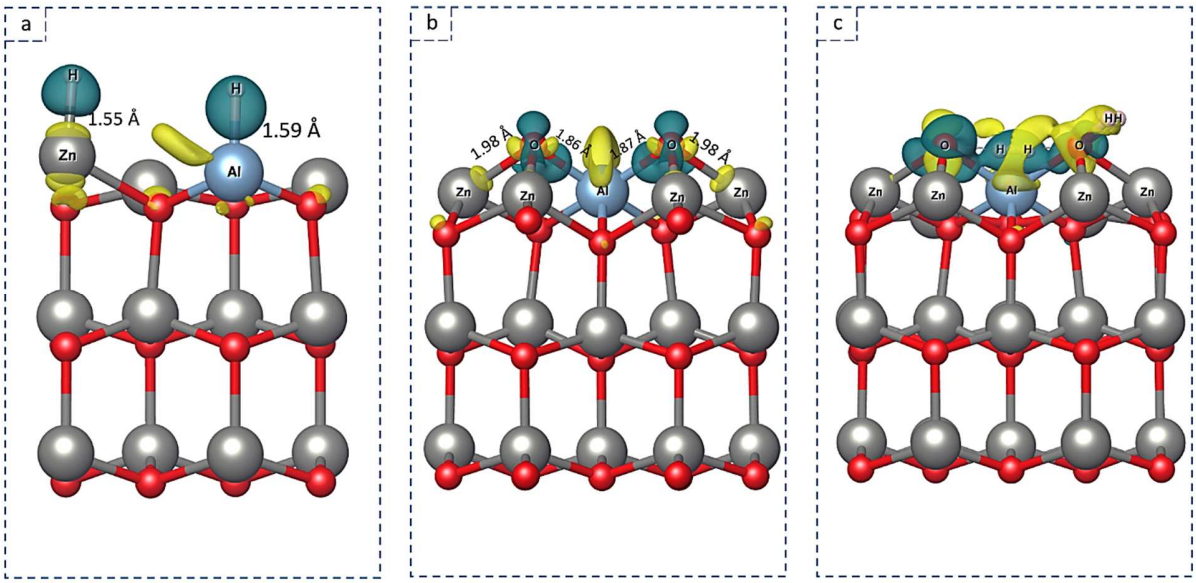

Figure 11. *Difference in electronic density ($\Delta\rho$) induced by the adsorption of a) H_2 b) O_2 on ZnO (0002) doped aluminum surface, c) the attack of H_2 on the adsorbed O_2. The blue (yellow) zones correspond to the increase (decrease) in density.*

3.2.4 Sn-doped ZnO

On the Sn-doped ZnO surface, the adsorption of the H_2 molecule showed similar behavior to that of pure ZnO. Herein, the total interaction energy is -17 kJ/mol, with an

interaction distance of 3.10 Å between hydrogen and Sn atoms. Comparing to H_2, the O_2 molecule is more adsorbed by around 20 kJ/mol. This adsorption led to a significant expansion of the O-O bond, from 1.20 to 1.52 Å, weakening this bond and proving the ability of Sn to facilitate the O_2 ion formation on the surface. All this occurs with a charge transfer of about 0.31 |e| and -0.63 |e|, respectively for Sn and O, which makes it favorable for hydrogen attack.

In the presence of the reducing gas, the H_2 molecule interacts with the adsorbed O ions, leading to the formation of the water molecule. Charge transfer analysis revealed that this process led to a full release (0.30 |e|) of the trapped electrons to Sn atoms. This indicates weak adsorption of H_2O on Sn-doped ZnO surface, and a significant increase of the doped material sensitivity toward H_2 gas, in line with the experiment.

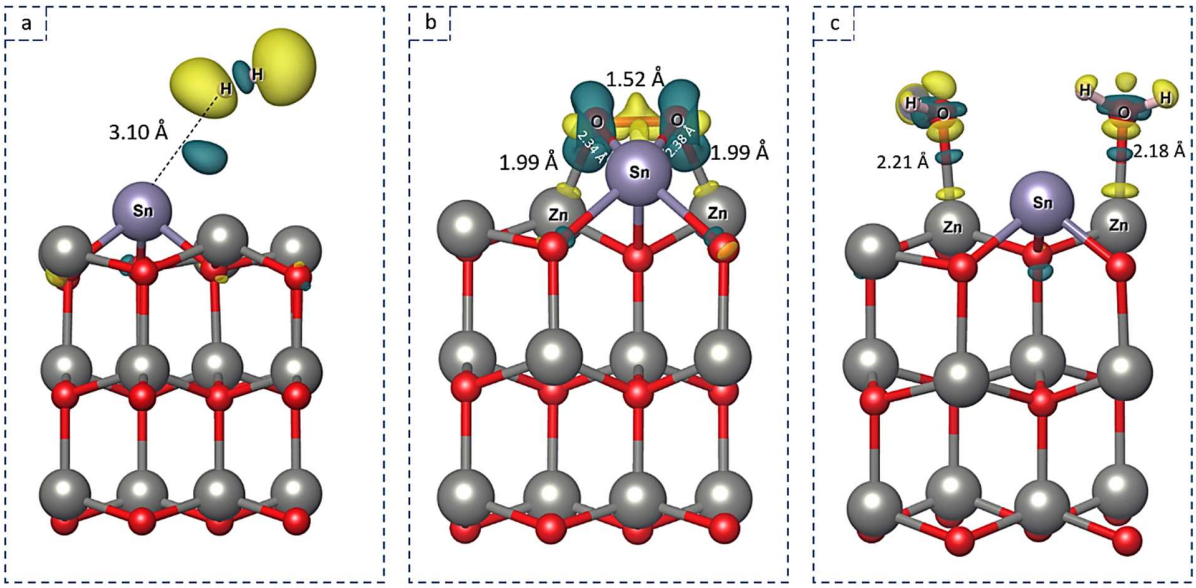

Figure 12. *Difference in electronic density (Δρ) induced by the adsorption of a) H_2 b) O_2 on ZnO (0002) doped tin surface, c) the attack of H_2 on the adsorbed O_2. The blue (yellow) zones indicate density increase (decrease).*

4. Conclusion

ZnO doped Al and Sn sensors were successfully synthesized. The experimental characterization showed the adequate surface for the adsorption phenomenon, especially for ZnO doped Sn followed by ZnO and ZnO doped Al that exhibited the lowest response. This low response was analyzed by the theoretical calculations using DFT. The influence of Sn and Al on the sensitivity of the Polar ZnO (0002) surface toward H_2 gas was studied experimentally and by DFT theoretical calculations. We observed that no H_2O formation has occurred on ZnO-Al surface and the charge transfer analysis showed that H_2 reaction with the oxygen molecule adsorbed on Al-doped ZnO can only release a 0.08 |e| back to the surface. Thus, H_2 gas cannot be detected. After Sn doping on the surface of ZnO (0002), it levels up from the surface and extends its Sn-O distance to reach 2.15 Å compared to that of pure Zn (1.92 Å). Then O_2 molecules of air are adsorbed on the ZnO-Sn surface weakening the O-O bond which makes it a favorable site for H_2 gas attack and H_2O formation leading to a full release of the trapped electrons. thus, an important enhancement in the detection of H_2 gas is observed, this agrees with the experimental results.

References

[1] A. Mirzaei, H.R. Yousefi, F. Falsafi, M. Bonyani, J.-H. Lee, J.-H. Kim, H.W. Kim, S.S. Kim, An overview on how Pd on resistive-based nanomaterial gas sensors can enhance response toward hydrogen gas, International Journal of Hydrogen Energy. 44 (2019) 20552–20571. https://doi.org/10.1016/j.ijhydene.2019.05.180.

[2] A.M. Abdalla, S. Hossain, O.B. Nisfindy, A.T. Azad, M. Dawood, A.K. Azad, Hydrogen production, storage, transportation and key challenges with applications: A review, Energy Conversion and Management. 165 (2018) 602–627. https://doi.org/10.1016/j.enconman.2018.03.088.

[3] G. Korotcenkov, S.D. Han, J.R. Stetter, Review of Electrochemical Hydrogen Sensors, Chem. Rev. 109 (2009) 1402–1433. https://doi.org/10.1021/cr800339k.

[4] S. Kabcum, D. Channei, A. Tuantranont, A. Wisitsoraat, C. Liewhiran, S. Phanichphant, Ultra-responsive hydrogen gas sensors based on PdO nanoparticle-decorated WO3 nanorods synthesized by precipitation and impregnation methods, Sensors and Actuators B: Chemical. 226 (2016) 76–89. https://doi.org/10.1016/j.snb.2015.11.120.

[5] A. Esfandiar, A. Irajizad, O. Akhavan, S. Ghasemi, M.R. Gholami, Pd–WO3/reduced graphene oxide hierarchical nanostructures as efficient hydrogen gas sensors, International Journal of Hydrogen Energy. 39 (2014) 8169–8179. https://doi.org/10.1016/j.ijhydene.2014.03.117.

[6] F.E. Annanouch, Z. Haddi, M. Ling, F. Di Maggio, S. Vallejos, T. Vilic, Y. Zhu, T. Shujah, P. Umek, C. Bittencourt, C. Blackman, E. Llobet, Aerosol-Assisted CVD-Grown PdO Nanoparticle-Decorated Tungsten Oxide Nanoneedles Extremely Sensitive and Selective to Hydrogen, ACS Appl. Mater. Interfaces. 8 (2016) 10413–10421. https://doi.org/10.1021/acsami.6b00773.

[7] J. Mizsei, Forty Years of Adventure with Semiconductor Gas Sensors, Procedia Engineering. 168 (2016) 221–226. https://doi.org/10.1016/j.proeng.2016.11.167.

[8] M. Hijazi, M. Rieu, V. Stambouli, G. Tournier, J.-P. Viricelle, C. Pijolat, Ambient temperature selective ammonia gas sensor based on SnO2-APTES modifications, Sensors and Actuators B: Chemical. 256 (2018) 440–447. https://doi.org/10.1016/j.snb.2017.10.036.
[9] O. Alev, E. Şennik, N. Kılınç, Z.Z. Öztürk, Gas Sensor Application of Hydrothermally Growth TiO2 Nanorods, Procedia Engineering. 120 (2015) 1162–1165. https://doi.org/10.1016/j.proeng.2015.08.747.
[10] U.T. Nakate, R. Ahmad, P. Patil, Y.T. Yu, Y.-B. Hahn, Ultra thin NiO nanosheets for high performance hydrogen gas sensor device, Applied Surface Science. 506 (2020) 144971. https://doi.org/10.1016/j.apsusc.2019.144971.
[11] Z. Zang, X. Tang, Enhanced fluorescence imaging performance of hydrophobic colloidal ZnO nanoparticles by a facile method, Journal of Alloys and Compounds. 619 (2015) 98–101. https://doi.org/10.1016/j.jallcom.2014.09.072.
[12] S.I. Boyadjiev, V. Georgieva, R. Yordanov, Z. Raicheva, I.M. Szilágyi, Preparation and characterization of ALD deposited ZnO thin films studied for gas sensors, Applied Surface Science. 387 (2016) 1230–1235. https://doi.org/10.1016/j.apsusc.2016.06.007.
[13] P.-W. Chi, C.-W. Su, D.-H. Wei, Control of hydrophobic surface and wetting states in ultra-flat ZnO films by GLAD method, Applied Surface Science. 404 (2017) 380–387. https://doi.org/10.1016/j.apsusc.2017.01.266.
[14] S.K. Singh, P. Tripathi, I. Sulania, V.V.S. Kumar, P. Kumar, Tuning the optical and electrical properties of magnetron-sputtered Cu–ZnO thin films using low energy Ar ion irradiation, Optical Materials. 114 (2021) 110985. https://doi.org/10.1016/j.optmat.2021.110985.
[15] Y. Köseoğlu, A simple microwave-assisted combustion synthesis and structural, optical and magnetic characterization of ZnO nanoplatelets, Ceramics International. 40 (2014) 4673–4679. https://doi.org/10.1016/j.ceramint.2013.09.008.
[16] A. Tiwari, P.P. Sahay, The effects of Sn–In co-doping on the structural, optical, photoluminescence and electrical characteristics of the sol-gel processed ZnO thin films, Optical Materials. 110 (2020) 110395. https://doi.org/10.1016/j.optmat.2020.110395.
[17] D.N. Sree, S.P.M. Deborrah, C. Gopinathan, S.S.R. Inbanathan, Enhanced UV light induced photocatalytic degradation of Methyl Orange by Fe doped spray pyrolysis deposited ZnO thin films, Applied Surface Science. 494 (2019) 116–123. https://doi.org/10.1016/j.apsusc.2019.07.091.
[18] G. Kumar, X. Li, Y. Du, Y. Geng, X. Hong, UV-light enhanced high sensitive hydrogen (H2) sensor based on spherical Au nanoparticles on ZnO nano-structured thin films, Journal of Alloys and Compounds. 798 (2019) 467–477. https://doi.org/10.1016/j.jallcom.2019.05.227.
[19] E. Della Gaspera, M. Guglielmi, A. Martucci, L. Giancaterini, C. Cantalini, Enhanced optical and electrical gas sensing response of sol–gel based NiO–Au and ZnO–Au nanostructured thin films, Sensors and Actuators B: Chemical. 164 (2012) 54–63. https://doi.org/10.1016/j.snb.2012.01.062.
[20] P. Papagiorgis, A. Stavrinadis, A. Othonos, G. Konstantatos, G. Itskos, The Influence of Doping on the Optoelectronic Properties of PbS Colloidal Quantum Dot Solids, Scientific Reports. 6 (2016) 18735. https://doi.org/10.1038/srep18735.
[21] R. Yoo, S. Cho, M.-J. Song, W. Lee, Highly sensitive gas sensor based on Al-doped ZnO nanoparticles for detection of dimethyl methylphosphonate as a chemical warfare agent simulant, Sensors and Actuators B: Chemical. 221 (2015) 217–223. https://doi.org/10.1016/j.snb.2015.06.076.
[22] Y.-H. Zhang, Y.-L. Li, F.-L. Gong, K.-F. Xie, M. Liu, H.-L. Zhang, S.-M. Fang, Al doped narcissus-like ZnO for enhanced NO2 sensing performance: An experimental and DFT investigation, Sensors and Actuators B: Chemical. 305 (2020) 127489. https://doi.org/10.1016/j.snb.2019.127489.
[23] Z.E. Khalidi, S. Fadili, B. Hartiti, A. Lfakir, P. Thevenin, M. Siadat, Behavior of NiO thin films sprayed at different annealing time, Opt Quant Electron. 48 (2016) 427. https://doi.org/10.1007/s11082-016-0694-8.
[24] H. Jabraoui, I. Khalil, S. Lebègue, M. Badawi, Ab initio screening of cation-exchanged zeolites for biofuel purification, Mol. Syst. Des. Eng. 4 (2019) 882–892. https://doi.org/10.1039/C9ME00015A.
[25] I. Khalil, H. Jabraoui, G. Maurin, S. Lebègue, M. Badawi, K. Thomas, F. Maugé, Selective Capture of Phenol from Biofuel Using Protonated Faujasite Zeolites with Different Si/Al Ratios, J. Phys. Chem. C. 122 (2018) 26419–26429. https://doi.org/10.1021/acs.jpcc.8b07875.
[26] I. Khalil, H. Jabraoui, S. Lebègue, W.J. Kim, L.-J. Aguilera, K. Thomas, F. Maugé, M. Badawi, Biofuel purification: Coupling experimental and theoretical investigations for efficient separation of phenol from

aromatics by zeolites, Chemical Engineering Journal. 402 (2020) 126264. https://doi.org/10.1016/j.cej.2020.126264.
[27] P. Hohenberg, W. Kohn, Inhomogeneous Electron Gas, Phys. Rev. 136 (1964) B864–B871. https://doi.org/10.1103/PhysRev.136.B864.
[28] L.J. Sham, W. Kohn, One-Particle Properties of an Inhomogeneous Interacting Electron Gas, Phys. Rev. 145 (1966) 561–567. https://doi.org/10.1103/PhysRev.145.561.
[29] G. Kresse, J. Furthmüller, Efficient iterative schemes for ab initio total-energy calculations using a plane-wave basis set, Phys. Rev. B. 54 (1996) 11169–11186. https://doi.org/10.1103/PhysRevB.54.11169.
[30] G. Kresse, J. Hafner, Ab initio molecular dynamics for liquid metals, Phys. Rev. B. 47 (1993) 558–561. https://doi.org/10.1103/PhysRevB.47.558.
[31] P.E. Blöchl, O. Jepsen, O.K. Andersen, Improved tetrahedron method for Brillouin-zone integrations, Phys. Rev. B. 49 (1994) 16223–16233. https://doi.org/10.1103/PhysRevB.49.16223.
[32] G. Kresse, J. Hafner, Norm-conserving and ultrasoft pseudopotentials for first-row and transition elements, J. Phys.: Condens. Matter. 6 (1994) 8245–8257. https://doi.org/10.1088/0953-8984/6/40/015.
[33] J.P. Perdew, K. Burke, M. Ernzerhof, Generalized Gradient Approximation Made Simple, Phys. Rev. Lett. 77 (1996) 3865–3868. https://doi.org/10.1103/PhysRevLett.77.3865.
[34] H. Jabraoui, E.P. Hessou, S. Chibani, L. Cantrel, S. Lebègue, M. Badawi, Adsorption of volatile organic and iodine compounds over silver-exchanged mordenites: A comparative periodic DFT study for several silver loadings, Applied Surface Science. 485 (2019) 56–63. https://doi.org/10.1016/j.apsusc.2019.03.282.
[35] W. Kohn, L.J. Sham, Self-Consistent Equations Including Exchange and Correlation Effects, Phys. Rev. 140 (1965) A1133–A1138. https://doi.org/10.1103/PhysRev.140.A1133.
[36] E.P. Hessou, H. Jabraoui, I. Khalil, M.-A. Dziurla, M. Badawi, Ab initio screening of zeolite Y formulations for efficient adsorption of thiophene in presence of benzene, Applied Surface Science. 541 (2021) 148515. https://doi.org/10.1016/j.apsusc.2020.148515.
[37] H. Jabraoui, T. Charpentier, S. Gin, J.-M. Delaye, R. Pollet, Atomic Insights into the Events Governing the Borosilicate Glass–Water Interface, J. Phys. Chem. C. 125 (2021) 7919–7931. https://doi.org/10.1021/acs.jpcc.1c00388.
[38] E.P. Hessou, L.A. Bédé, H. Jabraoui, A. Semmeq, M. Badawi, V. Valtchev, Adsorption of Toluene and Water over Cationic-Exchanged Y Zeolites: A DFT Exploration, Molecules. 26 (2021) 5486. https://doi.org/10.3390/molecules26185486.
[39] W. Tang, E. Sanville, G. Henkelman, A grid-based Bader analysis algorithm without lattice bias, J. Phys.: Condens. Matter. 21 (2009) 084204. https://doi.org/10.1088/0953-8984/21/8/084204.
[40] E. Sanville, S.D. Kenny, R. Smith, G. Henkelman, Improved grid-based algorithm for Bader charge allocation, J Comput Chem. 28 (2007) 899–908. https://doi.org/10.1002/jcc.20575.
[41] G. Henkelman, A. Arnaldsson, H. Jónsson, A fast and robust algorithm for Bader decomposition of charge density, Computational Materials Science. 36 (2006) 354–360. https://doi.org/10.1016/j.commatsci.2005.04.010.
[42] K. Momma, F. Izumi, VESTA: a three-dimensional visualization system for electronic and structural analysis, Journal of Applied Crystallography. 41 (2008) 653–658. https://doi.org/10.1107/S0021889808012016.
[43] E.P. Hessou, H. Jabraoui, M.T.A.K. Hounguè, J.-B. Mensah, M. Pastore, M. Badawi, A first principle evaluation of the adsorption mechanism and stability of volatile organic compounds into NaY zeolite, Zeitschrift Für Kristallographie - Crystalline Materials. 234 (2019) 469–482. https://doi.org/10.1515/zkri-2019-0003.
[44] K.A. Alim, V.A. Fonoberov, M. Shamsa, A.A. Balandin, Micro-Raman investigation of optical phonons in ZnO nanocrystals, Journal of Applied Physics. 97 (2005) 124313. https://doi.org/10.1063/1.1944222.
[45] C. Lin, Y. Zhao, G. Yin, Calculation of the lattice constant of solids with the use of valence electron structure parameters, Computational Materials Science. 97 (2015) 86–93. https://doi.org/10.1016/j.commatsci.2014.10.008.
[46] A.L. Patterson, The Scherrer Formula for X-Ray Particle Size Determination, Phys. Rev. 56 (1939) 978–982. https://doi.org/10.1103/PhysRev.56.978.
[47] S. Gao, M. Fivel, A. Ma, A. Hartmaier, 3D discrete dislocation dynamics study of creep behavior in Ni-base single crystal superalloys by a combined dislocation climb and vacancy diffusion model, Journal of the Mechanics and Physics of Solids. 102 (2017) 209–223. https://doi.org/10.1016/j.jmps.2017.02.010.

[48] M.H. Aslan, A.Y. Oral, E. Menşur, A. Gül, E. Başaran, Preparation of c-axis-oriented zinc-oxide thin films and the study of their microstructure and optical properties, Solar Energy Materials and Solar Cells. 82 (2004) 543–552. https://doi.org/10.1016/j.solmat.2003.06.016.
[49] U. Pal, J.G. Serrano, P. Santiago, G. Xiong, K.B. Ucer, R.T. Williams, Synthesis and optical properties of ZnO nanostructures with different morphologies, Optical Materials. 29 (2006) 65–69. https://doi.org/10.1016/j.optmat.2006.03.015.
[50] D.G. Mead, G.R. Wilkinson, The temperature dependence of the raman effect in some wurtzite type crystals, Journal of Raman Spectroscopy. 6 (1977) 123–129. https://doi.org/10.1002/jrs.1250060305.
[51] V.I. Nefedov, M.N. Firsov, I.S. Shaplygin, Electronic structures of MRhO2, MRh2O4, RhMO4 and Rh2MO6 on the basis of X-ray spectroscopy and ESCA data, Journal of Electron Spectroscopy and Related Phenomena. 26 (1982) 65–78. https://doi.org/10.1016/0368-2048(82)87006-0.
[52] R. Sankar ganesh, M. Navaneethan, G.K. Mani, S. Ponnusamy, K. Tsuchiya, C. Muthamizhchelvan, S. Kawasaki, Y. Hayakawa, Influence of Al doping on the structural, morphological, optical, and gas sensing properties of ZnO nanorods, Journal of Alloys and Compounds. 698 (2017) 555–564. https://doi.org/10.1016/j.jallcom.2016.12.187.
[53] T.T.D. Nguyen, D. Van Dao, I.-H. Lee, Y.-T. Yu, S.-Y. Oh, High response and selectivity toward hydrogen gas detection by In2O3 doped Pd@ZnO core-shell nanoparticles, Journal of Alloys and Compounds. 854 (2021) 157280. https://doi.org/10.1016/j.jallcom.2020.157280.
[54] Q.A. Drmosh, Z.H. Yamani, Hydrogen sensing properties of sputtered ZnO films decorated with Pt nanoparticles, Ceramics International. 42 (2016) 12378–12384. https://doi.org/10.1016/j.ceramint.2016.05.011.
[55] A.S. Mokrushin, I.A. Nagornov, T.L. Simonenko, N.P. Simonenko, P. Yu. Gorobtsov, T.V. Khamova, G.P. Kopitsa, A.N. Evzrezov, E.P. Simonenko, V.G. Sevastyanov, N.T. Kuznetsov, Chemoresistive gas-sensitive ZnO/Pt nanocomposites films applied by microplotter printing with increased sensitivity to benzene and hydrogen, Materials Science and Engineering: B. 271 (2021) 115233. https://doi.org/10.1016/j.mseb.2021.115233.
[56] O. Dulub, U. Diebold, G. Kresse, Novel Stabilization Mechanism on Polar Surfaces: ZnO(0001)-Zn, Phys. Rev. Lett. 90 (2003) 016102. https://doi.org/10.1103/PhysRevLett.90.016102.
[57] S.J. Pearton, D.P. Norton, K. Ip, Y.W. Heo, T. Steiner, Recent advances in processing of ZnO, Journal of Vacuum Science & Technology B: Microelectronics and Nanometer Structures Processing, Measurement, and Phenomena. 22 (2004) 932–948. https://doi.org/10.1116/1.1714985.